Characterization of an Extruded Mg-Dy-Nd Alloy during Stress Corrosion with C-Ring Tests

Petra Maier [1,*] **, Benjamin Clausius** [1] **, Jens Wicke** [1] **and Norbert Hort** [2]

[1] School of Mechanical Engineering, University of Applied Sciences Stralsund, 18435 Stralsund, Germany; benjamin.clausius@hochschule-stralsund.de (B.C.); jens.wicke@fh-stralsund.de (J.W.)

[2] Helmholtz-Zentrum Geesthacht, Magnesium Innovation Center, 21502 Geesthacht, Germany; norbert.hort@hzg.de

* Correspondence: petra.maier@hochschule-stralsund.de; Tel.: +49-3831-456419

check for updates

Abstract: This study focuses on the characterization of the failure behavior of an extruded Mg10Dy1Nd alloy during stress corrosion. The microstructure, hardness, strength and corrosion behavior of binary alloys Mg10Dy and Mg1Nd are compared to those of the ternary alloy system. The ternary alloy Mg-Dy-Nd that is not fully recrystallized has the highest hardness but lacks ductility. The investigated alloys twin during plastic deformation. Static C-ring tests in Ringer solution were used to evaluate the stress corrosion properties, and stress corrosion could not be found. None of the alloys failed by fracturing, but corrosion pits formed to various extents. These corrosion pits were elliptical in shape and located below the surface. Some of the pits reduced the remaining wall thickness significantly, but the stress increased by the notch effect did not lead to crack initiation. Furthermore, the C-ring specimen was subjected to compressive loading until fracture. Whereas the Mg1Nd alloy showed ductile behavior, the alloys containing Dy fractured on the tensile side. The crack initiation and growth were mainly influenced by the twin boundaries. The Mg10Dy1Nd alloy had an inhomogeneous microstructure and low ductility, which resulted in a lower fracture toughness than that of the Mg10Dy alloy. There were features that indicate hydrogen-assisted fracture. Although adding Nd decreased the fracture toughness, it reduced the grain size and had a positive influence on the corrosion rate during immersion testing.

Keywords: magnesium; Mg-Dy-Nd; C-ring test; stress corrosion; corrosion morphology

1. Introduction

Temporary implants made of biodegradable magnesium have been widely accepted; the challenges are known, and first applications are already in use [1–6]. Regarding the regeneration of musculoskeletal tissue, Mg alloys seem to be promising for customized engineering of degradable implants [7]. Biomechanical approaches have shown that a degraded Mg pin is well connected with bone [8], and the understanding of the degradation layer is increasing [9]. WE43, a rare earth-containing alloy (primarily Nd), is a high-strength alloy with an acceptable biologic response when the grain size is controlled to be very small [10–12]. According to the available data, WE43 does not show significant toxicity to living cells [12]. Although WE43 was originally developed as a creep-resistant alloy for aerospace applications, the alloys in this study are binary and ternary base alloys for Resoloy®, which was developed by MEKO Laser Materials Processing, Sarstedt, Germany and the Helmholtz Center Geesthacht, Geesthacht, Germany, specifically for absorbable implants [13–16]. Resoloy®is an alloy based on Mg-Dy-Nd with additional alloying elements Zn and Zr that showed excellent strength, ductility and corrosion behavior with an optimized microstructure, as demonstrated in previous

literature reports [17]. To eliminate Zn and Zr from Resoloy®, the alloy system Mg-Dy-Nd and its combinations are the focus of this study and used for comparison.

Research by Yang et al. [18] showed that the binary cast Mg-Dy alloy exhibits the best combination of mechanical and corrosion properties with 10 wt% Dy when alloying Dy between 5 and 20 wt%. Dy has a very high solubility in Mg (25.3 wt%) and alloying with Dy can adjust both the mechanical and corrosion properties by heat treatment; Dy alloys and its Dy-enriched corrosion layer also show good cytocompatibility, according to an in vitro study of the cytotoxicity and inflammatory response [19,20]. In situ solidification experiments on Mg20Dy found $Mg_{24}Dy_5$ as a secondary phase [21]. The equilibrium β phase has also been studied by Li et al. [22] and Smola et al. [23], and an aging response with an increase in hardness has been found. Nd has a low solid solubility in Mg and forms stable intermetallic phases at grain boundaries; therefore, it is added to provide precipitation strengthening. It also improves the corrosion resistance of Mg alloys by reducing the effect of galvanic corrosion between the secondary phases and the matrix and by providing an improved protective surface film. Furthermore, a Nd-implanted WE43 alloy exhibited a remarkably enhanced cell adhesion and biocompatibility [24–27]. A study on Mg2Nd demonstrated good in vivo biocompatibility and histological analysis showed moderate mucosal hyperplasia with a mild, nonspecific inflammatory response [27,28]. In addition to alloying Nd, Zn and Zr in Mg-Dy alloys, as is done in Resoloy® [17], combinations of Al, Zn, Zr [29] and Gd and Zr [30] have also been explored, mostly to tailor the mechanical and corrosion properties by heat treatment.

A uniform corrosion morphology, a moderate corrosion rate and low hydrogen evolution are required in biodegradable implant materials. The corrosion morphology is often described by the appearance of local corrosion: the amount, size and shape of corrosion pits. According to guidance by the ASTM, pitting can be examined by visual inspection using cross-sectional micrographs [31]. Harmful pits are deep and narrow, causing a strong reduction in the cross-sectional area and an increased stress intensity during mechanical loading; these pits act as notches and therefore as crack initiators. Harmless pits are wide and shallow; if they overlap during corrosion, a uniform corrosion morphology develops. Furthermore, the pitting factor resulting from the deepest corrosion pits in relation to the average corrosion rate is used to describe the corrosion morphology [32]. The relationship between the maximum local corrosion of the most intense pit and the average corrosion all over is determined by cross-sectional micrographs providing the deepest corrosion pit and the corrosion rate from the immersion test. Pitting factor equivalent of 1 showed uniform corrosion.

Some magnesium alloys are susceptible to stress corrosion cracking due to their inherent reactivity in aqueous environments, resulting in the production of hydrogen, but certain alloying elements increase the stress corrosion cracking (SCC) resistance [33,34]. According to Choudhary et al. [10], ZX50 suffers greater SCC than WZ21 and WE43. This was attributed to its higher susceptibility towards localized corrosion in m-SBF. The SCC mechanism for these alloys was the combination of hydrogen-assisted cracking (major contribution of SCC in WE43) and anodic dissolution (predominant mechanism for WZ21 alloy). Another study by Kannan et al. [35] showed an increased resistance to SCC in both distilled water and 0.5 wt% NaCl solution for EV31A compared to ZE41 and QE22. Intergranular SCC in a 0.5 wt% NaCl solution was associated with the second-phase particles along grain boundaries. Rare earth elements, like Nd, can improve the SCC resistance of magnesium alloys, as seen in EV31A. A slow strain rate test indicated that EV31A was less susceptible to SCC than AZ91E [36]. Under the low intense loading of a constant load, EV31A was even found to be resistant. Fractography of EV31A showed little evidence of hydrogen embrittlement. There are no data found in the literature on stress corrosion or hydrogen embrittlement of Mg-Dy-Nd.

C-ring specimens are preferred for determining the susceptibility of alloys to SCC in forms like tubes, rods and bars in the short transverse direction [37–39]. A C-ring can be regarded as a metal O-ring with an open side or split rings. The specimens are typically bolt loaded to a constant strain or constant load, per ASTM G 338 [40]. The C-ring configuration results in a complex strain field with very high local strains: there is a gradient through the thickness, varying from a maximum tension on

one surface to a maximum compression on the opposite surface. This provides the ability to investigate microstructural differences between tensile and compressive deformation processes. According to ASTM G 338 [40], a bending load is applied to cause a tensile strain on the outer surface; however, a compression load (or tension load) is often used to describe the loading condition [41–43]. U-bend or C-ring tests are rarely applied to magnesium alloys. C-ring tests have been established as a useful quality control for brittle materials, like ceramic composites [44]. On the other hand, exceeding a deformation of 40% defines the ductile behavior of the tested material [43]. Higher plastic strains were observed near grain boundaries after stressing because the boundaries acted as a barrier to dislocation motion by slip [45]. Stress corrosion cracks are usually investigated by optical micrographs, but they can be investigated by advanced methods, like polychromatic X-ray microdiffraction [46] or 3D electron backscatter diffraction [42]. Ringer solution is often used when the corrosion behavior of biodegradable metals is of interest; it is found to be more aggressive than HBSS or DMEM [32,47,48]. This study aims to reveal the stress corrosion susceptibility of a Mg-Dy-Nd alloy, and the influence of the Nd alloying element is of particular interest. Furthermore, the influence of microstructural features, like twins and grain boundaries, on the fracture toughness, here evaluated as fracture energy, is studied and evaluated by the crack initiation and propagation.

2. Materials and Methods

2.1. Processing and Mechanical Testing

The Mg-Dy-Nd (Mg10Dy, Mg10Dy1Nd and Mg1Nd) alloys were cast at the Helmholtz Centre in Geesthacht, Germany. High purity Mg (99.94%) (MEL, UK) was melted in a mild steel crucible under a protective gas atmosphere (Ar + 2% SF_6). An amount of 10 wt% of pure Dy (99.5%) and 1 wt% of Nd (99.5%) (Grirem, Beijing, China) were added at a melt temperature of 720 °C. The melt was then mechanically stirred with a stirrer rotating at 200 rpm for 30 min. After a short annealing at 500 °C for 15 min, tubes were indirectly hot-extruded at the Extrusion Research and Development Center TU Berlin at an overall temperature of 400 °C, a ram speed of 1.5 mm/s and an extrusion ratio of 19:1. The outer diameter of the as-extruded tubes was 35 mm, and the wall thickness was 5 mm.

The chemical composition Dy was analyzed by using X-Ray micro fluorescence M4 Tornado (Bruker, Billerica, MA, USA), Nd by using a spark optical emission spectroscopy Spectrolab M12 Hybrid (Ametek-Spectro, Kleve, Germany) and the impurities Fe, Cu, Ni were analyzed by using atomic absorption spectrometry 240FS AA(Agilent, Santa Clara, CA, USA). The grain size was determined by the line intercept method with a cross-sectional micrograph obtained on a Leica DMi8 A (Leica Microsystems GmbH, Wetzlar, Germany), which was also used for micrographic investigations of the corrosion morphology and crack initiation and propagation.

The Vickers hardness (HV1 and HV0.2) was determined on the tube material with approximately 30 indents using a ZHU2.5 (ZwickRoell, Ulm, Germany), and the average value is reported. To evaluate the amount of strain hardening on the tensile and compressive sides as well as the neutral region of the C-rings (up to a displacement of 7 mm), the hardness was measured at a 60-degree angle opposite the C-ring opening, where the highest strain was expected and compared to that of the tube material. To analyze the fracture appearance in the crack openings on the surface of the C-rings, scanning electron microscopy (SEM) was performed with a Carl Zeiss EVO40 (Carl Zeiss Microscopy GmbH, Jena, Germany). The tensile properties were measured at room temperature with a TIRA test 28100 mechanical testing machine (Tira GmbH, Schalkau, Germany) at an initial speed of 0.45 mm/min that changed to 2.4 mm/min after elastic deformation. The samples had a gauge length of 20 mm and were 2 mm thick and 6 mm wide. The compression tests were performed on cylindrical samples with a height of 6 mm and a diameter of 4 mm.

2.2. Immersion and C-Ring Tests, Fracture Energy and Corrosion Morphology

Immersion tests were performed on tube segments with a width of 10 mm, outer diameter of 34 mm and wall thickness of 2 mm in 500 mL Ringer solution (2 samples of each alloy) at 37 °C. The weight loss was measured by removing the corrosion products with chromic acid. The mean corrosion rate (mm/a) was measured by using the following equation, where Δ m is the weight change in g, A is the surface area of the sample in cm^2, t is the immersion time in h (in our study, 7 days) and ρ is the density in g/cm^3:

$$CR_m = \frac{8.76 \times 10^4 \times \Delta m}{A \times t \times \rho} \tag{1}$$

C-ring samples with a width of 10 mm were machined from the extruded tubes with an outer diameter of 34 mm. The wall thickness was chosen to be 2 mm. Figure 1a shows their position in the initial extruded tubes according to [39] and the sketch in Figure 1b the related dimensions. A transition from tensile to compressive stresses from the outer to the inner surface developed in the C-rings upon loading. To evaluate the stiffness, the elastic-plastic transition, the amount of elastic energy (spring back) and ductility, a compressive load (also sometimes described as a bending load [39]) was applied to the C-rings (3 samples each) without corrosion media for up to 17 mm (geometrical restriction). The applied deformation speed was 2 mm/min. The force needed for the displacement was monitored. The deformation was calculated in% according to the deformation of the diameter [42] by setting the displacement (the initial height of 34 mm minus the height of the deformed C-ring) in relation to the initial height, which provided information on the ductility. A maximum deformation of 50% was possible. When a deformation of 40% is exceeded, the material is supposed to have ductile behavior. The following values were used to describe the fracture behavior: the force at which the fracture started (evaluated by the reduction in the force with increasing displacement), its displacement value and its resulting fracture energy (the area underneath the force-displacement curve during crack propagation up to its turning point towards the end of the curve). From the force-displacement curve, it was determined that a displacement of 7 mm was within the plastic region, so this value was used to investigate the influence of the plastic deformation (tensile and compressive strain hardening) on the extent of the corrosion and its morphology. For these associated investigations, the C-ring samples were compressed 7 mm in a testing machine, removed to relieve the spring back and then corroded over 7 days in 330 mL Ringer solution (3 samples each) at 37 °C. Before corrosion, the samples were cleaned in an ultrasonic bath in ethanol. For the stress corrosion tests with a sustained stress, the C-ring samples were elastically and plastically deformed in the POM (Polyoxymethylene) apparatus for up to a 7 mm displacement and kept for 20 days in 500 mL Ringer solution (3 samples each) at 37 °C (see sample in Figure 1c) by being clamped between 2 plates. The POM apparatus consisted of polymer plates and screws, which were designed to eliminate creep. The distance of 27 mm between the POM plates did not change during the test duration. Distilled water was used to cover the samples in the POM apparatus and was refilled every 5 days.
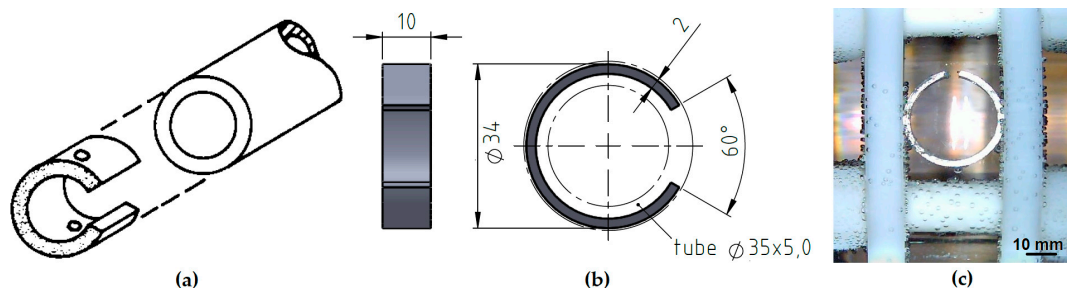

Figure 1. C-ring samples, position in the initial extruded tubes (**a**), sketch with dimensions (**b**) and during stress corrosion in the polyoxymethylene (POM) apparatus (**c**).

After the immersion tests, evaluation of the influence of the plastic deformation on the corrosion and stress corrosion, the C-rings were compressed under quasi-static loading in Ringer solution with a deformation speed of 2 mm/min, either up to fracturing or up to the geometrical restriction of 17 mm. These experiments enabled the influence of the corrosion media and possible hydrogen embrittlement at a higher strain deformation to be tested under quasi-static loading. To evaluate the corrosion morphology, the corroded tubes from the immersion tests, the plastically deformed C-rings and the C-rings exposed to stress corrosion, all with a width of 10 mm, were "sectioned" transversely by grinding them down to 7.5 mm, 5 mm and finally to 2.5 mm. For each step, the corrosion morphology was determined from the micrographs and described according to ASTM G46–76 [30], which is a standard visual chart for the rating of pitting corrosion. The depth and width of the corrosion pits were used to describe the amount of corrosion behavior.

3. Results and Discussion

3.1. Microstructure and Mechanical Properties

The detailed chemical composition and impurity levels of the three hot-extruded alloys are listed in Table 1. The alloys differ in terms of their grain size and homogeneity. The transverse grain size of Mg10Dy1Nd (Figure 2a) was 33.6 ± 9.67 μm. This ternary alloy has not been fully recrystallized, and the extrusion direction can be seen by the alignment of the second phases and their small surrounding grains (see longitudinal microstructure in Figure 2d). Very few grains show deformation twins. The Mg10Dy alloy has a homogeneously recrystallized microstructure (Figure 2b,e) with a transverse grain size of 36.2 ± 10.2 μm. There was no significant difference between the transverse cross-section and the longitudinal microstructure (the extrusion direction is indicated by the vertical line). The microstructure was free of twin boundaries. The Mg1Nd alloy contains small grains with an average grain size of 20.1 ± 4.74 μm that were heavily twinned (Figure 2c,f). There was also no significant difference between the transverse cross-section and the longitudinal microstructure.

Table 1. Chemical composition and impurity level of the extruded alloys in wt%.

Alloy	Dy	Nd	Fe	Cu	Ni	Mg
Mg1Nd	-	0.96	0.003	0.0006	0.0001	balance
Mg10Dy	12.43	-	0.004	0.0010	0.0004	balance
Mg10Dy1Nd	13.07	0.90	0.006	0.0011	0.0002	balance
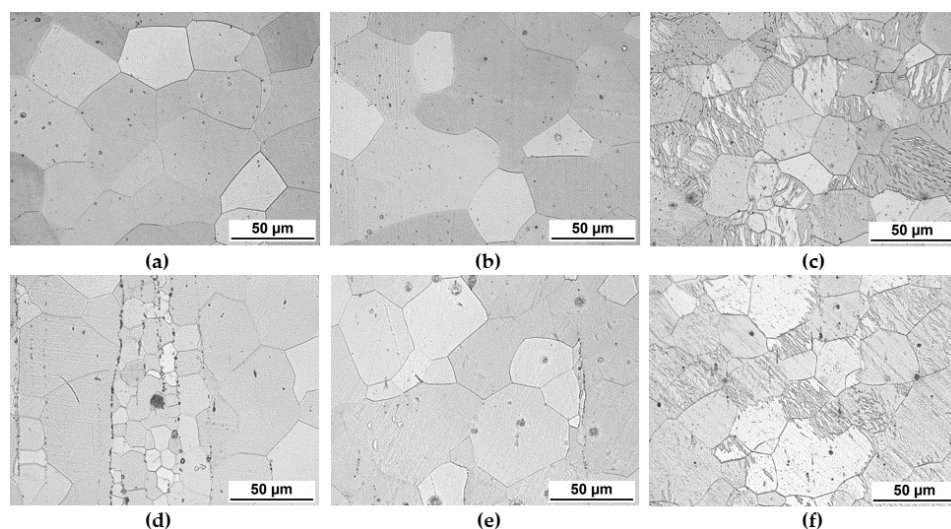
Figure 2. Optical micrographs of the Mg10Dy1Nd (**a**,**d**), Mg10Dy (**b**,**e**) and Mg1Nd (**c**,**f**) alloys. Transverse (**a**–**c**) and longitudinal cross sections, where the extrusion direction was vertical (**d**–**f**).

Although adding Nd reduces the average grain size, there was no significant positive effect on the tensile and compression properties (Figure 3a,b). The difference in the mechanical properties was very small, the values were within the range of the standard deviations. The average value of the tensile yield strength (TYS) at 0.2% for the Mg10Dy alloy was slightly higher than the average value for the Mg10Dy1Nd. However, the average values for TYS at 0.1%, ultimate tensile strength (UTS) and the stress values up to necking were slightly higher for the Mg10Dy1Nd alloy; the lower ductility caused the material to fail (see also Table 2.). The area containing the aligned second phases within the not fully recrystallized material that was shown in the longitudinal micrographs was assumed to be the area with an elevated brittleness and the area where the material started to fail. The Mg1Nd alloy was heavily twinned and showed an overall decreased tensile strength but elevated elongation to fracture. The average values of compression strength followed the same general trend. However, the average compression yield strength (CYS) at 0.1 and 0.2% for the Mg10Dy1Nd alloy was lower than that for the Mg10Dy alloy (which had the highest standard deviation herein), and the ultimate compression strength (UCS) was also slightly decreased (the stress up to necking was above that for the Mg10Dy alloy). The average elongation to compressive fracture (the compressive strain (CS)) was the lowest for the Mg10Dy1Nd alloy. Only the Mg1Nd alloy had a higher TYS at 0.2% than CYS at 0.2%, and the yield ratio (yield strength asymmetry = CYS/TYS) for the Mg10Dy and Mg10Dy1Nd alloys was above one, which was slightly elevated for the ternary alloy.
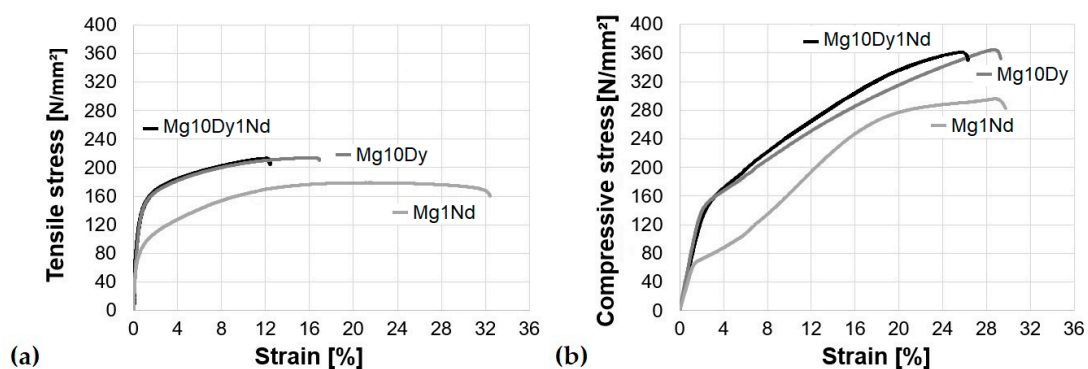

Figure 3. Stress–strain curves for the Mg10Dy1Nd, Mg10Dy and Mg1Nd alloys under tension (**a**) and compression (**b**).

Table 2. Tensile and compressive properties and yield strength asymmetry of the extruded alloys.

Alloy	TYS (0.1%) (MPa)	TYS (0.2%) (MPa)	UTS (MPa)	El. (%)	CYS (0.1%) (MPa)	CYS (0.2%) (MPa)	UCS (MPa)	CS (%)	CYS/ TYS (0.2%)
Mg1Nd	60.5 ± 6.2	71.3 ± 4.9	178.7 ± 3.3	29.7 ± 2.5	62.9 ± 2.7	66.4 ± 1.4	301.8 ± 9.9	24.3 ± 1.3	0.93
Mg10Dy	83.5 ± 2.7	109.5 ± 2.6	215.0 ± 2.9	16.5 ± 2.0	119.1 ± 16.6	131.8 ± 9.4	351.9 ± 24.0	24.1 ± 2.1	1.20
Mg10Dy1Nd	86.4 ± 4.1	105.9 ± 3.7	216.9 ± 3.9	14.5 ± 2.2	114.6 ± 11.4	129.9 ± 6.0	347.8 ± 11.9	20.1 ± 0.4	1.23

Figure 4a shows the force-displacement curves from the compression testing of the C-rings up to a displacement of 17 mm. These results provide information about the stiffness (and resulting spring back) and evaluate the elastic-plastic region, the strain-hardening amount (slope in the plastic region) and the ductility. The Mg10Dy1Nd and Mg10Dy (all 3 curves run close to each other and are almost seen as one) alloys showed similar stiffness values, and the Mg10Dy alloy yielded at a decreased force, but both alloys showed a similar strain-hardening behavior. The Mg1Nd (all 3 curves also run close to each other and are almost seen as one) alloy showed a decreased stiffness and yielded at a decreased force. Even though there was a small grain size, which would increase the strength according to the

Hall-Petch relationship, the twinned microstructure, lack of solid solution strengthening of the Dy alloying element, and low Nd composition of only 1 wt% caused an elastic-plastic transition at low forces. Because of the low stiffness of the Mg1Nd alloy, the amount of spring back was the lowest herein. Because of the low stiffness, during the static load test to a displacement of 7 mm, the ratio of plastic to elastic deformation was higher than in the Dy-containing alloys. All three alloys showed a very ductile behavior under C-ring compression, and only the Mg10Dy1Nd alloy showed very small cracks (the longest crack was ~150 μm) on the surface of the tensile side. These cracks started just before 17 mm; see the reduction in force in Figure 4a (black curves). The Mg10Dy and Mg1Nd alloys were free of surface cracks.
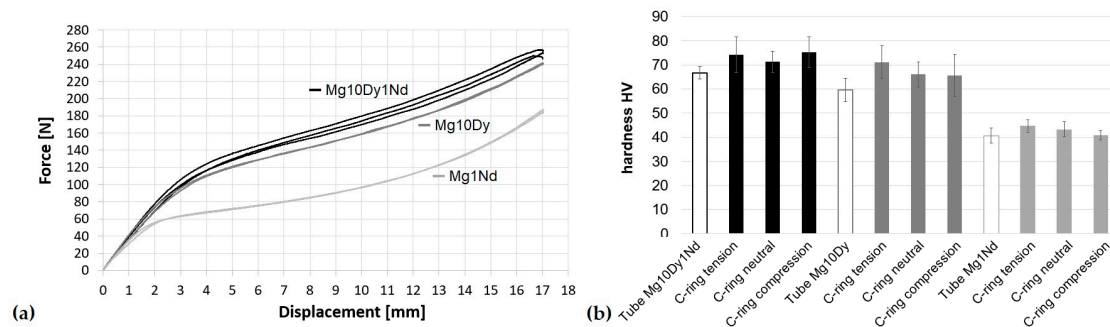

Figure 4. Force-displacement curves of C-ring tests of the Mg10Dy1Nd, Mg10Dy and Mg1Nd alloys (**a**) and hardness before and after C-ring tests up to a displacement of 7 mm (**b**).

The highest strength and hardness (see the hardness values of the tube materials in the open bars in Figure 4b) obtained herein for the Mg10Dy1Nd alloy may be explained by the high amount of Dy that caused solid solution strengthening and by the formation of stable intermetallic phases with Nd. The formation of the $Mg_{41}Nd_5$ equilibrium phase at the grain boundaries also decreases the grain size; the Mg10Dy1Nd alloy has a smaller average grain size than the Mg10Dy alloy. Up to a displacement of 7 mm, an average value of 145 N was needed for the Mg10Dy1Nd alloy and 130 N for the Mg10Dy alloy. Based on the mechanical properties evaluated from the C-ring compression at a 7 mm displacement and higher deformations, it can be seen that the Mg10Dy1Nd had a higher strength. The Mg10Dy alloy strength may have exceeded that for the Mg10Dy1Nd alloy had a deformation higher than 17 mm been possible (it was geometrically restricted here) and the force may have increased. The low ductility in the C-ring compression test-in agreement with tensile and compression tests-caused crack initiation in Mg10Dy1Nd before 17 mm. The force values at a 7 mm displacement allowed a comparison to Resoloy®in the as-extruded condition, which was studied in [17], and reveals a force of 180 N at a 7 mm displacement. The higher force needed for Resoloy®was mainly due to the grain refinement and formation of lamellar long-period stacking-ordered (LPSO) structures within the matrix when Zn and Zr were added.

Figure 4b shows the hardness values for the Mg10Dy1Nd, Mg10Dy and Mg1Nd alloys (for the extruded tubes and C-rings after plastic deformation at the tensile and compression side as well as neutral region and the amount of strain hardening during deformation of the C-rings in comparison to the extruded tubes by the increase in hardness. Pretesting showed that the transverse and longitudinal hardness of the tube material did not differ. All C-ring samples showed an increase in the hardness due to strain hardening during the C-ring tests. The increase on the tensile side was found to be the highest for the Mg10Dy alloy by 19.4% and the lowest for the Mg1Nd alloy by 9.7%. The average Mg10Dy1Nd strain hardening was slightly more increased on the compression side (12.8%) compared to that on the tensile side (11.2%). There was no pronounced strain hardening under compression in the Mg1Nd alloy according to the Vickers hardness: 0.4%. However, the stress–strain curve of the compression test showed significant hardening (Figure 3b). The twinned microstructure even before deformation influences the fact that the hardness did not show an increase. The Dy-containing alloys

were almost twin-free after extrusion and twin during plastic deformation during testing; the twinning in the Mg10Dy alloy was slightly elevated, especially on the compression side. The initial number of twins in the Mg1Nd alloy significantly increased during deformation on the tensile side, but only by a small band of approximately 100 μm. The hardness values of the tube material—and in general of the C-rings—agree with the data from the tension and compression tests within the uniform deformation region in addition to the data for the C-ring deformation strength.

3.2. Corrosion Rate and Morphology of the Stress Corrosion

The following corrosion rates were evaluated from immersion tests over 7 days: Mg10Dy1Nd corrodes at 1.53 mm/a, Mg10Dy at 2.46 mm/a and Mg1Nd at 0.79 mm/a. The twinned microstructure of Mg1Nd had no negative effect on the corrosion rate. Adding Nd to Mg10Dy lowers the corrosion rate. The electrochemical potential of Dy is −2.35 V, which is similar to that of Mg that has a value of −2.37 V. Dy in solid solution is not causing microgalvanic corrosion. The material in this study consisted of Mg-Dy and Mg-Dy-Nd second phases, like $Mg_{24}Dy_5$ and $Mg_5(Nd,Dy)$, which accelerate microgalvanic corrosion, compared to Mg1Nd and cause pitting corrosion. According to [18], the corrosion film is nonuniform and has a porous structure. A corrosion layer mainly consisting of MgO and $Mg(OH)_2$ can be easily penetrated by Cl-ions and was not effective [49]; the film was slightly improved when alloyed with Nd.

The cross-sectional micrographs in Figure 5 show the amount and size of the corrosion pits and that the Mg10Dy alloy (Figure 5b,e) corroded more severely under the influence of plastic deformation than the Mg10Dy1Nd (Figure 5a,d) and Mg1Nd alloys (Figure 5c,f). The largest corrosion pits on each alloy are shown. The Mg1Nd alloy exhibited evidence of corrosion but only has a few corrosion pits. Even the material was heavily twinned, an almost uniform passive layer prevented from strong corrosion and pitting. The pit seen in Figure 5f had an elliptical shape; its pitting factor was 4. Due to the number of twins, a stronger corrosion attack was expected. The area opposite the C-ring opening on the tensile side, where the highest strain was expected and the corrosion product could delaminate, was found to be corroded preferentially. The Mg10Dy alloy showed more and much larger corrosion pits than the Mg10Dy1Nd alloy. The pit on the Mg10Dy1Nd alloy in Figure 5a had a semicircle shape and starts to undercut the surface. Its pitting factor was 20. The pits in Mg10Dy were all subsurface, the ongoing corrosion overlapped, and the deepest accumulation of pits had a pitting factor of 23. Narrow and deep pits caused high stresses, and the pits in the Mg-Dy-(Nd) alloy were more wide than deep, causing a moderate stress intensity.
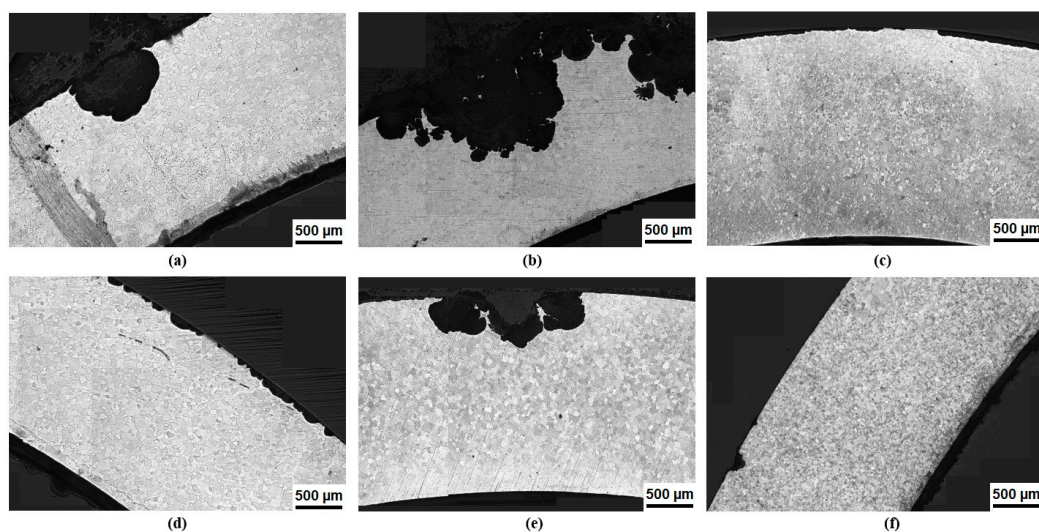

Figure 5. Optical micrographs of corroded C-rings after plastic deformation over 7 days for Mg10Dy1Nd (**a**,**d**), Mg10Dy (**b**,**e**) and Mg1Nd alloys (**c**,**f**).

Already by visual appearance of the Mg10Dy1Nd and Mg10Dy samples (not shown in this study) after the immersion tests, corrosion products were not formed uniformly, large accumulations of white corrosion products were seen. The area underneath the strong local formation of corrosion products was the one, where the pits have developed, see also [18,31]. Mg1Nd showed hardly any local corrosion products on the outer surface of the C-ring after 7 days. However, all samples had lost their metallic gloss.

Figure 6 shows representative micrographs of the C-rings after stress corrosion for over 20 days. It can be seen very clearly that the Mg10Dy alloy (Figure 6b,e) corroded the most and very severely on the tension and compression sides on both sides of the ring. Whereas the Mg10Dy1Nd alloy (Figure 6a,d) forms elliptical and semicircular pits (slightly subsurface) that started overlapping and the Mg10Dy alloy (Figure 6b,e) forms subsurface-undercutting pits. The corrosion of the Mg1Nd alloy after 20 days also increased; however, the number of pits was far less than that in the Dy-containing alloys, and the subsurface pits were not very deep and were rather wide. In agreement to the discussion above, the pits were formed, where the accumulation of corrosion product were found. The formation of these wide and shallow corrosion pits did not cause a significant stress increase when mechanical loading was applied. Because of the severe corrosion on the Mg10Dy alloy and the overlapped on both sides after 20 days, it was not possible to determine the pitting factor. The Mg10Dy1Nd alloy had a pitting factor of 37 and Mg1Nd has a factor of 15. These were very high and unacceptable values. The corrosion morphology, as shown in Figure 5c,d, was acceptable if the pits were not narrow and deep but overlapped to form a wide and shallow corrosion layer.
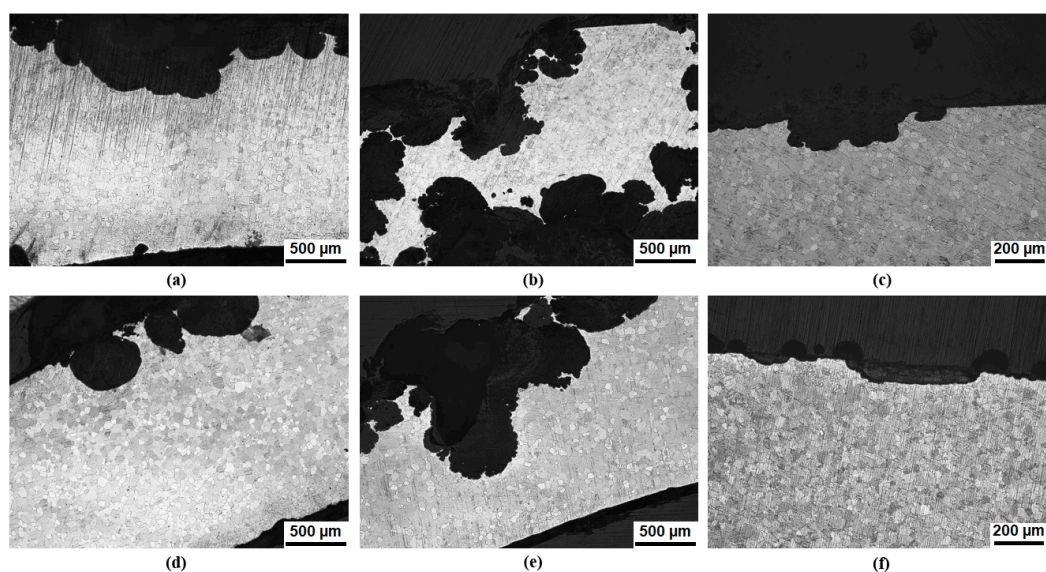

Figure 6. Optical micrographs of corroded C-rings after stress corrosion for over 20 days for the Mg10Dy1Nd (**a**,**d**), Mg10Dy (**b**,**e**) and Mg1Nd alloys (**c**,**f**).

Stress corrosion did not change the corrosion morphology significantly compared to that for the corrosion on samples that were only plastically deformed, but due to the increase in the corrosion time, the corrosion amount increased. All alloys investigated did not show a hint of stress corrosion cracking, and none of the alloys showed any crack initiation near the area where the pits had their deepest depth into the material.

3.3. Fracture Energy and Crack Propagation

Figure 7a shows the force–displacement curves of the C-rings under compressive loading in Ringer solution up to fracture for the Mg10Dy1Nd and Mg10Dy alloys and up to the geometrical restriction of 17 mm for the Mg1Nd alloy. The Mg10Dy1Nd alloy yielded at an elevated force and fractures at lower

displacements between 10 and 12 mm. With that, the average deformation to fracture was found to be approximately 32%. The binary alloy Mg10Dy started fracturing at 12 mm, but 2 C-rings reached values above 14 mm. The average deformation value was approximately 41%. According to [42], fracturing above 40% was defined as ductile failure. Alloy Mg1Nd showed a very ductile behavior, and the force-displacement curve did not give the appearance of a fracture or even crack initiation. Even though the microstructure was heavily twinned, the fine grains and low content of alloying prevent the Mg1Nd from fracturing. This alloy seemed to be resistant to hydrogen embrittlement, in contrast to the Mg10Dy and Mg10Dy1Nd alloys.
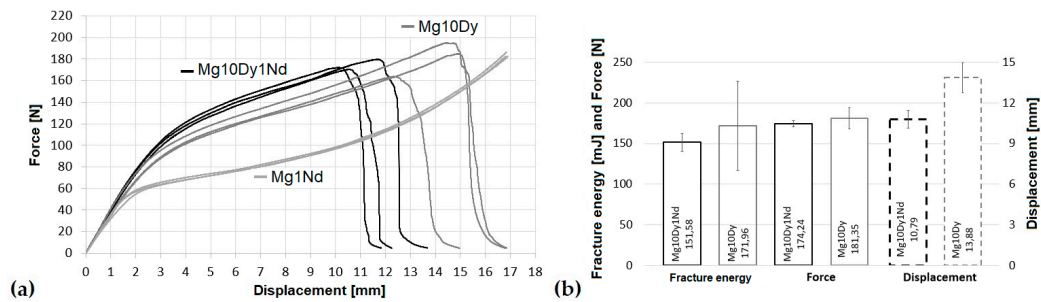

Figure 7. Force–displacement curves of C-rings tests under compressive loading in Ringer solution up to fracture for the Mg10Dy1Nd, Mg10Dy and Mg1Nd alloys (**a**) and their properties (**b**).

The following values have been used to describe the fracture behavior: the force at which the fracture started (evaluated by the reduction in the force with increasing displacement), its displacement value and the fracture energy (the area underneath the force–displacement curve during crack propagation). Figure 7b shows that the fracture energy and the displacement needed to initiate a crack were noticeably higher in the Mg10Dy alloy than in the Mg10Dy1Nd alloy, whereas the force needed to initiate a crack did not differ much. However, the force–displacement curve of the Mg10Dy1Nd alloy was elevated; see Figure 7a for data within the strain hardening region up to 10 mm; however, since alloy Mg10Dy1Nd has a low ductility, this alloy fractures at low displacement values. The high ductility of Mg10Dy allows the force to increase (see also properties from the tensile and compressive tests in Table 2). Therefore, the high fracture toughness in Mg10Dy was based on its high ductility. The elevated force values within the strain hardening region in the C-rings tests for the Mg10Dy alloy and its earlier fracture (Figure 7a) agree with values from tensile and compressive tests (see Figure 3a,b).

Figure 8 shows micrographs of the crack path in the C-ring samples after compressive loading in Ringer solution up to fracture. Figure 8a–c,g and h show the full wall thickness of the C-ring and Figure 8d–f,i–m show micrographs of higher magnification revealing detailed interaction of microstructure and crack growth. In the Mg10Dy1Nd (Figure 8a,d,g,k) and Mg10Dy alloys (Figure 8b,e,h,l), the crack propagates almost through the full wall thickness of the C-ring sample, and in alloy Mg1Nd (Figure 8c,f,i,m), only very small crack tips were seen (Figure 8i,m). According to the force-displacement curves in Figure 7a, these small cracks initiate without a noticeable drop in the force values. One characteristic of the crack paths in the Mg10Dy1Nd and Mg10Dy alloys (Figure 8a,b,g,h) was the change in appearance when they reached and crossed the neutral region: additional secondary cracks were developed, even at a distance from the main crack (and not connected in the chosen layer), and follow microstructural features, like twin boundaries (intragranular fracture). The cracks emanating from the main crack in parallel (see circled markers in Figure 8a,k) were assigned to the presence of hydrogen in [50]. The cracks were then carried over the grain boundaries by cleavage cracks, which were mostly twin-initiated, and the grain boundaries were not really part of the crack path. Twins will act as a potent stress concentrator in the nucleation of cracks, like seen in twinning-induced plasticity steels [51]. Most of the secondary microcracks grow within the grain by thickening before they propagate into the neighboring grain. That correlates to the shape of the twins, which become lenticular and indicate that the materials have a certain toughness. There was also favorable twin

transmission across the grain boundaries [52], where the twins grow from a common grain boundary (adjoining twin pairs). Some of these twins develop into cracks. Only a few twins and cracks were transmitted across the grain boundary without growing. The compressive side of the C-ring sample showed a very twinned microstructure. This region has an increased hardness, especially in alloy Mg10Dy1Nd (see Figure 4b). It was difficult to evaluate how the propagation of the crack tip through the twinned microstructure increases the fracture toughness because of unstable crack growth.
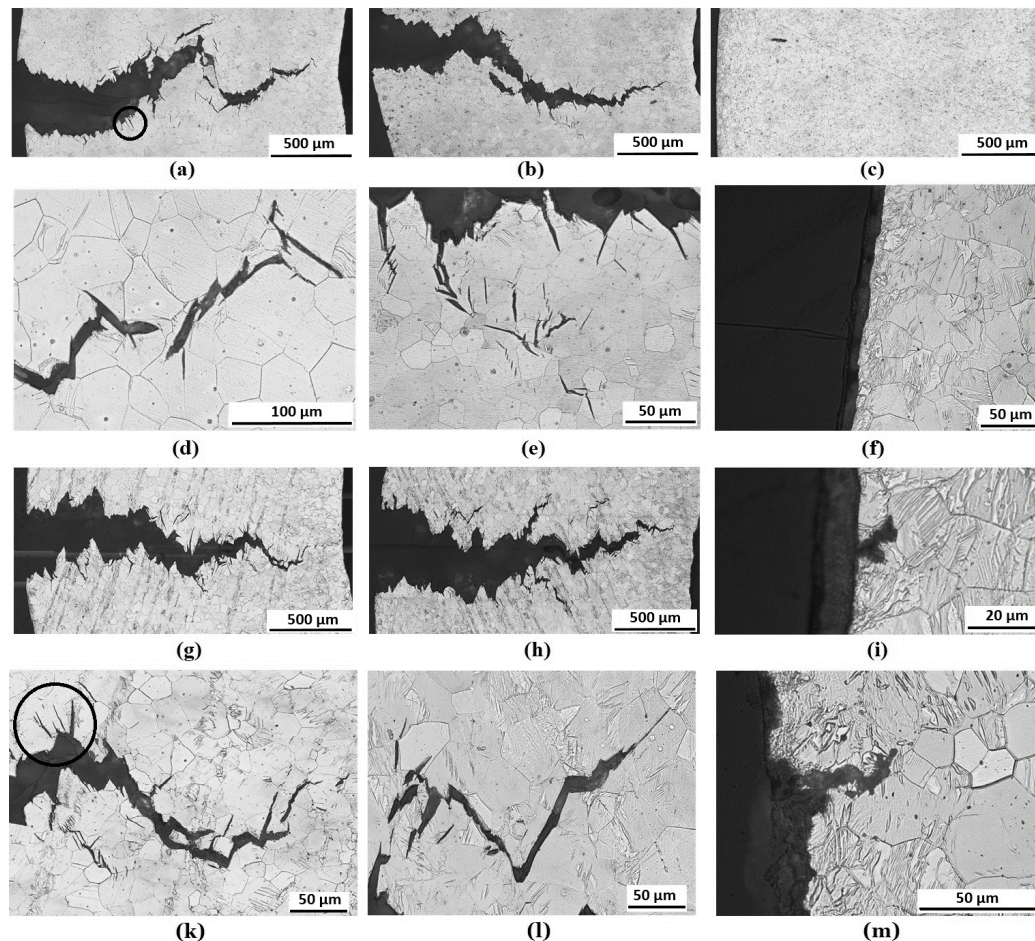
Figure 8. Cross-sectional optical micrographs of the crack path in the C-ring samples after compressive loading in Ringer solution: Mg10Dy1Nd (**a,d,g,k**), Mg10Dy (**b,e,h,l**) and Mg1Nd alloys (**c,f,i,m**). Micrographs showing full wall thickness of C-ring (**a–c,g,h**) and micrographs of higher magnification revealing detailed interaction of microstructure and crack growth (**d–f,i–m**), circled markers highlights parallel subcracks emanating from the main crack (**a,k**).

Figure 8d,e,k,l show the secondary cracks at a high magnification, indicating that the initiation was strongly influenced by the twin boundaries. Microstructural features, like grain and other twin boundaries as well as secondary phases, hinder straight crack propagation, redirect the crack up to the next interface and increase the fracture toughness. Twin boundaries seem to depress crack driving force, resulting in crack energy dissipation, retarding crack propagation. The influence of twins on the crack propagation has also been observed in Mg10Gd-based alloys [53]. In this study, where the as-cast Mg10Gd alloys with and without Nd have large grains up to 1000 µm in size, the alloys were tested by three-point bending. During this test, substantial crack reorientation (zigzag) by the twins occurs as a result of plastic deformation (the twin boundaries seem to "carry" the crack from grain to grain). Hydrogen-assisted failure in twinned areas, which cannot be excluded, has been mainly studied in twinning-induced plasticity steels, such as in Fe-Mn-C steels [54] but also in Mg alloys [55]. According

to [54], hydrogen-assisted cracking starts at a deformation twin boundary or a noncoherent grain boundary, where the propagation path aligns to a deformation twin boundary. In [55], the localized corrosion area in wrought Mg-Zn-Y-Zr was studied, where low surface energy planes accumulated hydrogen atoms and initiated cracks. Hydrogen is known to diffuse to lattice defects, like dislocations and twin boundaries. According to Figure 7b, the fracture energy was elevated in alloy Mg10Dy, which was mostly because of its elevated ductility. Upon studying the micrographs of crack propagation (Figure 8), it can be concluded that alloy Mg10Dy has an increasing number of large subcracks, which leads to the increase of fracture energy, and alloy Mg10Dy1Nd has a large number of small cracks that originate at the main crack. This explains the decreased resistivity to SCC in the Mg10Dy1Nd alloy; it was mostly based on low ductility, which makes it more susceptible to hydrogen embrittlement. A high ductility enlarges the deformation zone and energy in front of the crack tip, which allows deformation, such as dislocation movement, twinning and microcracking, before final fracture; these factors increase the fracture toughness. After all, the cracks initiated in alloy Mg10Dy1Nd during C-ring compression in air (Figure 3a) also show twin boundary cracking but at a decreased level. The parallel subcracks off the main crack according to [50] were not found. Testing in air also showed a very twinned microstructure on the tensile side, where hydrogen embrittlement was eliminated, and additional cold work occurs.

Figure 9 shows SEM images of cracks on the surface of the C-ring samples after compressive loading in Ringer solution. SEM images offer the view into the crack opening on the fracture surface and its area nearby to discuss the amount of corrosion products. Figure 9a to c show representative crack openings and their surrounding surface in the Mg10Dy1Nd, Mg10Dy and Mg1Nd alloys in an overview image. The extent of the small surface cracks in alloy Mg1Nd and the corroded surface nearby can be seen in the SEM images in Figure 9c,f. Other than seen in the immersion tests, the exposure of the C-ring during compression test in Ringer solution for over 8.5 min (17 mm displacement with 2 mm/min) caused significant corrosion at the crack opening in alloy Mg1Nd. The corrosion-product-free surface area surrounding the corrosion indicates that the local stress increase at the crack tip accelerates the corrosion process and formation of corrosion products at the outer surface of the C-ring and the fracture surface. The air-formed passive layer on the C-ring protects Mg1Nd during immersion, even the microstructure was heavily twinned (see smallest corrosion rate and uniform corrosion in Figure 5c for immersion over 7 days). Once the passive layer was channeled and broken, the twins in Mg1Nd seem to accelerate the corrosion (see here the strongly corroded fracture surface in Figure 9f).
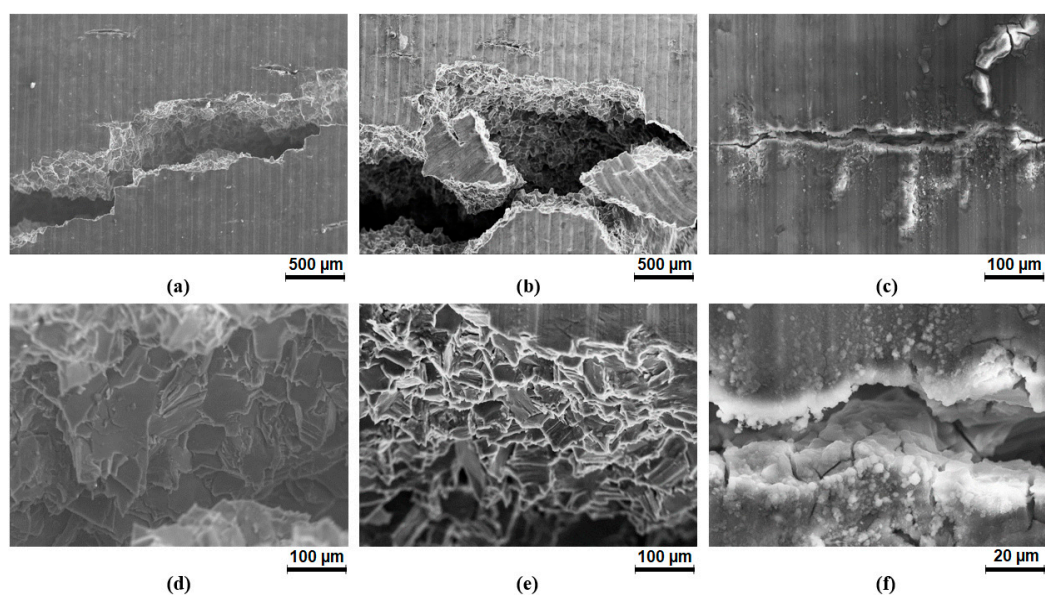

Figure 9. SEM images of the cracked surface of the C-rings after compressive loading in Ringer solution: Mg10Dy1Nd (**a**,**d**), Mg10Dy (**b**,**e**) and Mg1Nd alloys (**c**,**f**).

Figure 9a shows one main crack in alloy Mg10Dy1Nd and a few very small surrounding cracks, whereas the crack opening in alloy Mg10Dy in Figure 9b looks fairly severe with more than one main crack, which indicates an increased fracture toughness. It takes an average of 6.9 min to initiate a crack in alloy Mg10Dy and severe surface corrosion, C-ring outer surface and fracture surface, did not occur. The surface of alloy Mg10DyNd must be exposed to the solution for 5.4 min on average before crack initiation was also free of strong corrosion. This indicates that a rather sudden crack initiation occurs due to hydrogen embrittlement, whereas in alloy Mg1Nd, the local stress increase builds up over some time, accelerating the corrosion nearby (Figure 9c,f). Even the Dy-containing alloys have a higher corrosion rate due to a less protective and porous passive/corrosion layer, the fracture surface was free of corrosion. The smaller number of twins will be benefiting the situation.

Figure 9d,e show the fracture surface of Mg10Dy1Nd and Mg10Dy in a higher magnification and cleavage facets were present, which ascertain the transgranular crack propagation mode. Some cleavage planes show cleavage steps. Referring to the cross-sectional micrographs in Figure 8, this fracture mechanism was assisted by the deformation twin boundaries, underlining the crystallographic relationship on crack growth. Microcracks following twin boundaries and cleavage rivers being terminated by twin boundaries are also discussed by Smida and Bosansky in [56].

Future work will show whether the fracture toughness upon the addition of Zn and Zr alloying elements will be improved as it was for Resoloys®mechanical properties, like the hardness and force needed in C-ring tests. The reduced grain size and improved corrosion behavior due to the LPSO phase [17] is cause for optimism. Small grains and high-volume fraction of second phases are known to suppress twinning [53].

4. Conclusions

The mechanical and stress corrosion properties of ternary alloy Mg10Dy1Nd were obtained and compared to those for binary alloys Mg10Dy and Mg1Nd in this study. The microstructure, hardness, strength and corrosion behavior differ among the alloys. The following main conclusions can be made: Mg10Dy1Nd has not been fully recrystallized, has the highest hardness herein but lacks ductility. Mg1Nd was heavily twinned after extrusion and has the smallest grain size herein. The alloys twin under plastic deformation and the twinning was pronounced under compression. Mg10Dy corrodes at 2.46 mm/a, Mg10Dy1Nd at 1.53 mm/a and Mg1Nd at 0.79 mm/a. During static stress corrosion at a deformation of 20%, none of the alloys fail by fracturing, but large corrosion pits develop in alloy Mg10Dy1Nd and even more develop in alloy Mg10Dy. The pits were elliptical in shape and started to overlap. Wide and shallow pitting corrosion was identified for Mg1Nd. The C-ring specimen subjected to compressive loading until fracture in Ringer solution reveals a higher fracture toughness, evaluated as fracture energy, for Mg10Dy than that for the other alloys because of its ductility. Mg10Dy1Nd has a higher susceptibility to hydrogen embrittlement than the other alloys and Mg1Nd did not experience hydrogen-assisted fracture. The C-ring compression tests in Ringer solution show a deformation before fracture of 41% for alloy Mg10Dy and 32% for alloy Mg10Dy1Nd and crack initiation and growth were mainly influenced by twins.

References

1. Witte, F.; Hort, N.; Feyerabend, F.; Vogt, C. Magnesium (Mg) corrosion: A challenging concept for degradable implant. In *Corros. Magnes. Alloys*, 1st ed.; Song, G.L., Ed.; Woodhead Publishing Limited: Cambridge, UK, 2011; pp. 403–425. ISBN 978-1-84569-708-2.
2. Zheng, Y.F.; Gu, X.N.; Witte, F. Biodegradable metals. *Mat. Sci. Eng. R.* **2014**, *77*, 1–34. [CrossRef]
3. Li, H.; Zheng, Y.F.; Qin, L. Progress of biodegradable metals. *Progress in Nat. Sci.* **2014**, *24*, 414–422. [CrossRef]
4. Biotronik AG. Available online: www.biotronik.com/de-de/products/coronary/magmaris (accessed on 31 March 2020).
5. Seitz, J.M.; Lucas, A.; Kirschner, M. Magnesium-based compression screws: A novelty in the clinical use of implants. *JOM* **2016**, *68*, 1177–1182. [CrossRef]
6. Rahim, M.I.; Ullah, S.; Mueller, P. Advances and Challenges of Biodegradable Implant Materials with a Focus on Magnesium-Alloys and Bacterial Infections. *Metals* **2018**, *8*, 532. [CrossRef]
7. Prasadh, S.; Ratheesh, V.; Manakari, V.; Parande, G.; Gupta, M.; Wong, R. The Potential of Magnesium Based Materials in Mandibular Reconstruction. *Metals* **2019**, *9*, 302. [CrossRef]
8. Willumeit-Römer, R. The Interface between Degradable Mg and Tissue. *JOM* **2019**, *71*, 1447–1455. [CrossRef]
9. Angrisani, N.; Reifenrath, J.; Zimmermann, F.; Eifler, R.; Meyer-Lindenberg, A.; Vano-Herrera, K.; Vogt, C. Biocompatibility and degradation of LAE442-based magnesium alloys after implantation of up to 3.5 years in a rabbit model. *Acta Biomater.* **2016**, *44*, 355–365. [CrossRef]
10. Choudhary, L.; Singh Raman, R.K.; Hofstetter, J.; Uggowitzer, P.J. In-vitro characterization of stress corrosion cracking of aluminium-free magnesium alloys for temporary bio-implant applications. *Mater. Sci. Eng. C* **2014**, *42*, 629–636. [CrossRef]
11. Kang, Y.H.; Wu, D.; Chen, R.S.; Han, E.H. Microstructures and mechanical properties of the age hardened Mge4.2Ye2.5Nde1Gde0.6Zr (WE43) microalloyed with Zn. *J. Magnes Alloys* **2014**, *2*, 109–115. [CrossRef]
12. Dobatkin, S.; Martynenko, N.; Anisimova, N.; Kiselevskiy, M.; Prosvirnin, D.; Terentiev, V.; Yurchenko, N.; Salishchev, G.; Estrin, Y. Mechanical Properties, Biodegradation, and Biocompatibility of Ultrafine Grained Magnesium Alloy WE43. *Materials* **2019**, *12*, 3627. [CrossRef]
13. Stekker, M.; Hort, N.; Feyerabend, F.; Hoffmann, E. Magnesium Alloy and Resorbable Stents Containing the Same. U.S. Patent 9,566,367 B2, 14 February 2017.
14. Stekker, M.; Hort, N.; Feyerabend, F.; Hoffmann, E.; Hoffmann, M.; Horres, R. Resorbable Stents which Contain a Magnesium Alloy. U.S. Patent 9,522,219 B2, 20 December 2016.
15. Stekker, M.; Hort, N.; Feyerabend, F.; Hoffmann, E. Magnesiumlegierung Sowie Resorbierbare Stents, Welche Diese Enthalten. EU Patent 2744531, 21 October 2015.
16. Stekker, M.; Hort, N.; Feyerabend, F.; Hoffmann, E.; Hoffmann, M.; Horres, R. Resorbable Stents Containing a Magnesium Alloy. EU Patent 2744532, 16 September 2015.
17. Maier, P.; Steinacker, A.; Clausius, C.; Hort, N. Influence of solution heat treatment on microstructure, hardness and stress corrosion behaviour of extruded Resoloy®. *JOM* **2020**, *72*, 1870–1879. [CrossRef]
18. Yang, L.; Huang, Y.; Peng, Q.; Feyerabend, F.; Kainer, K.U.; Willumeit, R. Mechanical and corrosion properties of binary Mg–Dy alloys for medical applications. *Mater. Sci. Eng. B* **2011**, *176*, 1827–1834. [CrossRef]
19. Feyerabend, F.; Fischer, J.; Holtz, J.; Witte, F.; Willumeit, R.; Drücker, H.; Vogt, C.; Hort, N. Evaluation of short-term effects of rare earth and other elements used in magnesium alloys on primary cells and cell lines. *Acta Biomater.* **2010**, *6*, 1834–1842. [CrossRef] [PubMed]
20. Yang, L.; Hort, N.; Laipple, D.; Höche, D.; Huang, Y.; Kainer, K.U.; Willumeit, R.; Feyerabend, F. Element distribution in the corrosion layer and cytotoxicity of alloy Mg–10Dy during in vitro biodegradation. *Acta Biomater.* **2013**, *9*, 8475–8487. [CrossRef] [PubMed]
21. Tolnai, D.; Staron, P.; Staeck, A.; Eckerlebe, H.; Schell, N.; Müller, M.; Gröbner, J.; Hort, N. In Situ Synchrotron Radiation Diffraction of the Solidification of Mg-Dy(-Zr) Alloys. In *Magnesium Technology 2016*; Singh, A., Solanki, K., Manuel, M.V., Neelameggham, N.R., Eds.; Springer: Cham, Switzerland, 2016; pp. 17–21.
22. Li, D.; Dong, J.; Zeng, X.; Lu, C. Transmission electron microscopic investigation of the β1→β phase transformation in a Mg–Dy-Nd alloy. *Mater. Charact.* **2010**, *61*, 818–823. [CrossRef]
23. Smola, B.; Stulikova, I.; Cerna, J.; Cızek, J.; Vlach, M. Phase transformations in MgTbNd alloy. *Phys. Status Solidi A* **2011**, *208*, 2741–2748. [CrossRef]

24. Jin, W.; Wu, G.; Feng, H.; Wang, W.; Zhang, X.; Chu, P.K. Improvement of corrosion resistance and biocompatibility of rare-earth WE43 magnesium alloy by neodymium self-ion implantation. *Corros. Sci.* **2015**, *94*, 142–155. [CrossRef]

25. Zhang, T.; Meng, G.; Shao, Y.; Cui, Z.; Wang, F. Corrosion of hot extrusion AZ91 magnesium alloy. Part II: Effect of rare earth element neodymium (Nd) on the corrosion behavior of extruded alloy. *Corros. Sci.* **2011**, *53*, 2934–2942. [CrossRef]

26. Arrabal, R.; Pardo, A.; Merino, M.C.; Mohedano, M.; Casajús, P.; Paucar, K.; Garcés, G. Effect of Nd on the corrosion behaviour of AM50 and AZ91D magnesium alloys in 3.5 wt.% NaCl solution. *Corros. Sci.* **2012**, *55*, 301–312. [CrossRef]

27. Eifler, R.; Seitz, J.M.; Weber, C.M.; Grundke, S.; Reifenrath, J. MgNd2 alloy in contact with nasal mucosa: An in vivo and in vitro approach. *J. Mater. Sci.* **2016**, *27*, 25. [CrossRef]

28. Durisin, M.; Reifenrath, J.; Weber, C.M.; Eifler, R.; Maier, H.J.; Lenarz, T.; Seitz, J.M. Biodegradable nasal stents (MgF2-coated Mg–2 wt% Nd alloy)—A long-term in vivo study. *J. Biomed. Mater. Res. B* **2017**, *105*, 350–365. [CrossRef] [PubMed]

29. Kuncicka, L.; Kocich, R. Comprehensive Characterisation of a Newly Developed Mg–Dy–Al–Zn–Zr Alloy Structure. *Metals* **2018**, *8*, 73. [CrossRef]

30. Yang, L.; Huang, Y.; Feyerabend, F.; Willumeit, R.; Mendis, C.; Kainer, K.U.; Hort, N. Microstructure, mechanical and corrosion properties of Mg–Dy–Gd–Zr alloys for medical applications. *Acta Biomater.* **2013**, *9*, 8499–8508. [CrossRef] [PubMed]

31. ASTM International. *Standard Guide for Examination and Evaluation of Pitting Corrosion*; ASTM G46-94(2018); ASTM International: West Conshohocken, PA, USA, 2018. [CrossRef]

32. Maier, P.; Gentzsch, L.; Hort, N. Voltammetric Studies of Extruded Pure Magnesium in Different Electrolytes and Its Corrosion Morphology. In *Magnesium Technology*; Solanki, K., Orlov, D., Singh, A., Neelameggham, N., Eds.; Springer: Cham, Switzerland, 2017; pp. 429–437. [CrossRef]

33. Winzer, N.; Atrens, A.; Song, G.; Ghali, E.; Dietzel, W.; Kainer, K.U.; Hort, N.; Blawert, C. Critical Review of the Stress Corrosion Cracking (SCC) of Magnesium Alloys. *Adv. Eng. Mater.* **2005**, *7*, 659–693. [CrossRef]

34. Jafari, S.; Harandi, S.E.; Singh Raman, R.K. A Review of Stress-Corrosion Cracking and Corrosion Fatigue of Magnesium Alloys for Biodegradable Implant Applications. *JOM* **2015**, *67*, 1143–1153. [CrossRef]

35. Kannan, M.B.; Dietzel, W.; Blawert, C.; Atrens, A.; Lyon, P. Stress corrosion cracking of rare-earth-containing magnesium alloys ZE41, QE22 and Elektron 21 (EV31A) compared with AZ80. *Mater. Sci. Eng. A* **2007**, *480*, 529–539. [CrossRef]

36. Padekar, B.S.; Singh Raman, R.K.; Raja, V.S.; Paul, P. Stress corrosion cracking of a recent rare-earth containing magnesium alloy, EV31A, and a common Al-containing alloy, AZ91E. *Corros. Sci.* **2013**, *71*, 1–9. [CrossRef]

37. Koch, G.H. Tests for Stress-Corrosion. *Adv. Mater. Process.* **2001**, *159*, 36–38.

38. Singh, R. Corrosion evaluation and monitoring practices. In *Training Programme on Industrial Corrosion: Evaluation and Mitigation*; NML: Jamshedpur, India, 2017; pp. 48–67.

39. Rutkowski, B.; Malzbender, J.; Beck, T.; Steinbrech, R.W.; Singheiser, L. Creep behaviour of tubular Ba0.5Sr0.5Co0.8Fe0.2O3−δ gas separation membranes. *J. Eur. Ceram. Soc.* **2011**, *31*, 493–499. [CrossRef]

40. ASTM International. *Standard Practice for Making and Using C-Ring Stress-Corrosion Test Specimens*; ASTM G38-01(2013); ASTM International: West Conshohocken, PA, USA, 2013. [CrossRef]

41. Procopio, A.T.; Zavaliangos, A.; Cunningham, J.C. Analysis of the diametrical compression test and the applicability to plastically deforming materials. *J. Mat. Sci.* **2003**, *38*, 3629–3639. [CrossRef]

42. Gillen, C.; Garner, A.; Plowman, A.; Race, C.P.; Lowe, T.; Jones, C.; Moore, K.L.; Frankel, P. Advanced 3D characterisation of iodine induced stress corrosion cracks in zirconium alloys. *Mater. Charact.* **2018**, *141*, 348–361. [CrossRef]

43. Wilczynska, K.; Bono, M.; Le Boulch, D.; Fregonese, M.; Chabretou, V.; Mozzani, N.; Rautenberg, M. Simulation of C-Ring, O-Ring and tensile ring specimens for Iodine induced Stress Corrosion Cracking experiments on zirconium alloy. In *Proceedings of EUROCORR Congress*; European Federation of Corrosion: Krakau, Polen, 2018; p. 110972.

44. Jacobsen, G.M.; Stone, J.D.; Khalifa, H.E.; Deck, C.P.; Back, C.A. Investigation of the C-ring test for measuring hoop tensile strength of nuclear grade ceramic composites. *J. Nucl. Mater.* **2014**, *452*, 125–132. [CrossRef]

45. McIntyre, N.S.; Ulaganathan, J.; Simpson, T.; Qin, J.; Sherry, N.; Bauer, M.; Carcea, A.G.; Newman, R.C.; Kunz, M.; Tamura, N. Mapping of Microscopic Strain Distributions in an Alloy 600 C-Ring After Application of Hoop Stresses and Stress Corrosion Cracking. *Corrosion* **2014**, *70*, 66–73. [CrossRef]

46. Chao, J.; Suominen-Fuller, M.L.; McIntyre, N.S.; Carcea, A.G.; Newman, R.C.; Kunz, M.; Tamura, N. The study of stress application and corrosion cracking on Ni–16 Cr–9 Fe (Alloy 600) C-ring samples by polychromatic X-ray microdiffraction. *Acta Mater.* **2012**, *60*, 781–792. [CrossRef]

47. Feliu, S.; Veleva, L.; García-Galvan, F. Effect of Temperature on the Corrosion Behavior of Biodegradable AZ31B Magnesium Alloy in Ringer's Physiological Solution. *Metals* **2019**, *9*, 591. [CrossRef]

48. Mueller, W.D. Electrochemical techniques for assessment of corrosion behaviour of Mg and Mg-alloys. *BIO Nano Mater.* **2015**, *16*, 31–39. [CrossRef]

49. Song, G.; Atrens, A. Understanding Magnesium Corrosion: A Framework for improved alloy performance. *Adv. Eng. Mater.* **2003**, *5*, 837–858. [CrossRef]

50. Sozańska, M.; Mościcki, A.; Czujko, T. The Characterization of Stress Corrosion Cracking in the AE44 Magnesium Casting Alloy Using Quantitative Fractography Methods. *Materials* **2019**, *12*, 4125. [CrossRef]

51. Luo, Z.C.; Liu, R.D.; Wang, X.; Huang, M.X. The effect of deformation twins on the quasi-cleavage crack propagation in twinning-induced plasticity steels. *Acta Mater.* **2018**, *150*, 59–68. [CrossRef]

52. Arul Kumar, M.; Capolungo, L.; McCabe, R.J.; Tomé, C.N. Characterizing the role of adjoining twins at grain boundaries in hexagonal close packed materials. *Sci. Rep.* **2019**, *9*, 3846. [CrossRef]

53. Maier, P.; Mendis, C.L.; Wolff, M.; Hort, N. Twinning assisted crack propagation of Magnesium-Rare Earth casting and wrought alloys under bending. *Mater. Sci. Forum* **2015**, *828*, 217–311. [CrossRef]

54. Koyama, M.; Akiyama, E.; Tsuzaki, K.; Raabe, D. Hydrogen-assisted failure in a twinning-induced plasticity steel studied under in situ hydrogen charging by electron channeling contrast imaging. *Acta Mater.* **2013**, *61*, 4607–4618. [CrossRef]

55. Wang, S.D.; Xu, D.K.; Chen, X.B.; Han, E.H.; Dong, C. Effect of heat treatment on the corrosion resistance and mechanical properties of an as-forged Mg–Zn–Y–Zr alloy. *Corros. Sci.* **2015**, *92*, 228–236. [CrossRef]

56. Smida, T.; Bosansky, J. Micromechanism of cleavage fracture in ferritic steels. *Kov. Mater.* **2002**, *40*, 146–160.